

Master's Thesis

Machine Learning Models for z -Reconstruction in DarkSide-20k Experiment

Noelia Vicente López

September 2025



**UNIVERSIDAD
DE GRANADA**

Supervision: Miguel Cárdenas-Montes, Roberto Santorelli

CIEMAT (Centro de Investigaciones Energéticas, Medioambientales y Tecnológicas)

Supervisors Signature:

Contents

Abstract	3
1 Introduction	4
2 Direct Detection of WIMP-DM	6
2.1 Gravitational Evidence of Dark Matter	6
2.1.1 Galactic scale	6
2.1.2 Cosmological scale	7
2.2 General Properties and Candidates of Dark Matter	7
2.3 WIMP-Nucleus Interactions	9
2.4 Current Status	10
2.4.1 Xe vs Ar	11
3 The DarkSide-20k Experiment	13
3.1 Background Events and Mitigation Strategies	13
3.2 The DS-20k Detector	14
3.3 Light Production in Liquid Argon	15
3.4 The Pile-up Problem	15
4 S1 z-Reconstruction	17
4.1 Used data	17
4.2 Neural Networks and Deep Learning	19
4.2.1 Multilayer Perceptron	19
4.2.2 Convolutional Neural Networks	21
4.3 Results	22
4.3.1 Dataset Description	22
4.3.2 Results for 1D input	22
4.3.3 Results for 2D input	22
5 Conclusion	25
References	26

Abstract

DarkSide-20k will be a dual-phase Liquid Argon (LAr) Time Projection Chamber (TPC) with 50 t (total mass of UAr) for direct WIMP search under ultra-low background conditions. It provides access to both scintillation (S1) and electron (S2) signals produced by particle interaction in the LAr target. The DarkSide-20k experiment will be the most advanced and largest liquid argon TPC ever built for dark matter searches. Due to the inherently slow drift of ionization electrons in such detectors, overlapping events (pile-up) can occur when multiple interactions happen within the same drift time window, posing significant challenges for event reconstruction. When multiple events occur close in time, their S2 signals may overlap, making it difficult to identify which S2 corresponds to which S1. By estimating the z -coordinate directly from the S1 light pattern, it becomes possible to predict when the associated S2 should appear, thus enabling correct matching and reducing the impact of pile-up — namely, the risk of rejecting valid events or introducing dead time in the detector readout. This work explores deep network-based algorithms for position reconstruction in this detector, improving models by learning features. Two different approaches are used: Multilayer Perceptrons (MLPs) and Convolutional Neural Networks (CNNs) to incorporate the spatial distribution of sensors. The best result achieved so far is a 32 cm error in the z -coordinate. These are initial steps toward position reconstruction in pile-up scenarios. Ongoing improvements and comparisons with other methods are underway.

Keywords: DarkSide-20k, LAr TPC, WIMP detection, pile-up mitigation, deep learning.

1 Introduction

The nature of dark matter (DM) is an open question in modern physics. Several astrophysical observations from various scales provide strong evidence of its existence and constrain some basic properties. Recent results indicate that the mass-energy content of the universe is nearly 68.5% dark energy, 26.5% DM, and 4.9% visible (or baryonic) matter [1].

One possibility is that dark matter consists of new particles outside the Standard Model (SM) of particle physics, which are thermal relics of the Big Bang. In the dominant paradigm, these particles were non-relativistic at the time of decoupling, as stated by the Lambda Cold Dark Matter (Λ CDM) model. An attractive solution for the “missing mass” problem is a Weakly Interacting Massive Particle (WIMP), motivated by supersymmetry (SUSY), which only interact via gravity and by definition the weak force, making them difficult to detect.

The WIMP discovery would provide key insights into the structure and dynamics of the universe, offering clues to “new physics” beyond the SM (BSM). Experimental efforts employ three complementary strategies: direct detection using shielded underground detectors, indirect detection with telescopes and other astronomical instruments, and high-energy collider experiments. None have yet yielded conclusive results, so it is necessary to reach new levels of sensitivity, improving current limits by a few orders of magnitude.

At the LHC, the ATLAS and CMS experiments search for hidden channels in pp collisions with high missing transverse momentum, significantly greater than that expected from neutrinos, which could indicate WIMPs escaping the detectors. Indirect detection looks for final states from annihilation (or decay) channels in high DM density regions, seeking excesses in antiparticle fluxes (PAMELA, AMS), γ -rays (Fermi-LAT, MAGIC) and neutrinos (IceCube, Super-Kamiokande) relative to the cosmic background. Given the model dependence and the difficulty in isolating astrophysical sources of radiation, direct searches on Earth are the most straightforward path of identification.

Direct detection experiments aim to observe rare, low-energy (keV-scale) nuclear recoils produced by the elastic scattering of galactic WIMPs — dark matter particles from the Milky Way halo — off target nuclei. These interactions are expected to occur at extremely low rates, requiring detectors to operate under ultra-low background conditions to ensure unambiguous identification. A relevant factor is the choice of detector technology and target. Noble liquid detectors are currently at the forefront of direct dark matter searches, offering high sensitivity to WIMPs in the mass range from 10 GeV to several TeV. Thanks to their efficient scintillation and ionization responses, as well as their scalability to multi-ton volumes, they allow for low energy thresholds and can probe spin-independent WIMP-nucleon cross sections down to the 10^{-47} cm² level — surpassing previous experimental limits by orders of magnitude. For liquid argon (LAr), pulse shape discrimination (PSD) against background, precise event xyz -position determination in the TPC layout, and high radio-purity levels have been demonstrated.

In this view, the Global Argon Dark Matter Collaboration (GADMC) proposes a unified program for LAr-DM direct detection with the DarkSide-20k experiment (DS-20k, 200 t yr planned exposure) and its successor, ARGO-300 (Argo, 3000 t yr). DS-20k, a background-free (< 0.1 events) dual-phase LAr TPC detector using scintillation (S1) and electroluminescence (S2) signals, plans to reach a 90% C.L. exclusion sensitivity to WIMP-nucleon cross sections of 6.3×10^{-48} cm² for 1 TeV WIMPs over 10 yr run in a fiducial volume. This is a factor of approximately 3 improvement over the currently published limits [2], [3].

Increasing the detector volume boosts the event rate but introduces challenges such as event pile-up, where overlapping ionization signals from multiple recoils recorded simultaneously complicate the distinction of single events and lead to their rejection. This work proposes deep learning models for event vertex z -reconstruction from the S1 signal in DS-20k, improving the S1-S2 association and mitigating pile-up losses. A successful DS-20k detector would advance the next generation multi-ton detectors with sensitivities near the *neutrino fog* and higher exposure.

2 Direct Detection of WIMP-DM

Direct detection experiments aim to observe the rare elastic scattering of galactic dark matter particles — WIMPs from the Milky Way halo — off atomic nuclei in terrestrial detectors. Assuming a local dark matter density of $\rho_{\text{DM}} = 0.3 \text{ GeV/cm}^3$ [4], these particles may occasionally interact with the target as the Earth moves through the halo, producing low-energy (keV-scale) nuclear recoils. To detect such rare events, experiments are operated deep underground and optimized for ultra-low backgrounds, minimizing interference from cosmic rays and natural radioactivity.

In this chapter, the most compelling and well-known gravitational observations in favor of a DM component are first discussed from a historical perspective (Section 2.1). The main physical constraints and some widely probed DM models are then reviewed (Section 2.2). Finally, the standard WIMP scenario is examined, exploring the detection principles and the current status of direct detection efforts (Sections 2.3 and 2.4).

2.1 Gravitational Evidence of Dark Matter

The existence of DM is inferred through gravity, as seen in the rotational curves of galaxies, the dynamics of colliding galaxy clusters, and the cosmic microwave background (CMB). Further evidence comes from gravitational lensing, where the curvature of space-time bends light near massive bodies, allowing us to map the distribution of DM in distant galaxies. These observations point to the presence of additional matter in the universe that is non-luminous, neither emitting nor absorbing electromagnetic (EM) radiation, and non-baryonic, to explain the discrepancies observed when applying known physics.

2.1.1 Galactic scale

Dark matter was proposed in the 1930s by astronomers J.H. Oort [5], through his study of the Doppler shifts of stars near the plane of the Milky Way, and F. Zwicky [6], who measured the velocity dispersion $\sigma(v)$ of galaxies in the Coma and Virgo clusters using the virial theorem. Both concluded that there must be an overabundance of non-visible matter, or dark matter.

In galaxies, most of the visible mass is clustered at the center. For a given density profile $\rho(r)$, the Gauss theorem predicts that, outside the galactic core, the gravitational pull follows $\propto M/r^2$, where $M = M(r)$ is the integrated mass within the visible orbit, and r is the galactocentric distance. This force provides a centripetal acceleration $\propto v^2/r$ for bodies orbiting the galaxy center, implying that the velocity of stars and other galactic objects is given by

$$v(r) = \sqrt{\frac{GM(r)}{r}}, \quad (1)$$

which shows that, at large radii, the distribution of visible matter exhibits a “Keplerian decline”.

In the 1970s, Vera Rubin [7] observed the Doppler shifts of spectral lines in a catalog of nearly 60 spiral galaxies to infer their orbital velocities. Rubin notably found that the velocity profiles $v(r)$ always lie largely above the expected behavior coming from the independent quantification of the visible galactic mass from mass-to-luminosity ratio of stars and non-luminous (gaseous or solid) mass. This confirmed that Zwicky’s conclusions could be extended to the

galactic scale. The preferred explanation for this discrepancy assumes the existence of a larger DM halo around galaxies, extending beyond the visible and rotating stars. However, the specific details of the profile of this DM distribution remain unclear.

Another strong piece of evidence for DM came from the 2006 observation by Douglas et al. [8] of 1E 0657-558 (the “Bullet” cluster), the merger of two galaxy clusters. The major component of a cluster’s mass is intergalactic gas, which interacts via EM forces and can be observed through its predominant emission in the X-ray band. The gravitational lensing and X-ray observations show that, during the collision, visible matter and hypothetical DM interact differently: the two DM halos passed through one another without interacting, while the baryonic gas was shocked and located between the two halos. This sets an upper limit on the small DM self-interaction cross section to $\sigma_{\text{DM-DM}}/m_{\text{DM}} < 1.25 \text{ cm}^2 \text{ g}^{-1}$ (68 C.L.) [9]. The latest analysis of Chandra and Hubble data, based on 72 galactic cluster collisions, gives $\sigma_{\text{DM-DM}}/m_{\text{DM}} \leq 0.47 \text{ cm}^2 \text{ g}^{-1}$ (95 C.L.) [10].

2.1.2 Cosmological scale

The Λ CDM cosmological model assumes that the universe began from a singularity called “Big Bang”, and predicts its composition as a combination of dark energy (parameterized by the cosmological constant Λ), ordinary matter, and cold dark matter (CDM). Although this model is widely accepted, many issues remain unresolved, including the missing satellites, cusp-core, and too-big-to-fail problems.

Dark matter is not only *dark* but also cold and non-baryonic, as strongly implied by the simulations of observed large-scale structure in the universe, fluctuations in the CMB, and big bang nucleosynthesis (BBN). It must travel at non-relativistic speeds at the time of decoupling, or else it would prevent structure formation below the galactic cluster scale and produce a smaller relic abundance than that inferred from fits to the CMB power spectrum. The CDM scenario can be easily realized with heavy and collision-less particles. If massless or much lighter, dark matter should have some interaction properties, or some coherent aggregation, that is sufficient to simulate a non-relativistic gravitational clustering that drives early structure formation. In currently known physics, only massive particles have the energy to inflict a significant gravitational pull.

The best estimate to date is that $(83.9 \pm 1.5)\%$ of the matter in the universe is dark matter, based on measurements of tiny fluctuations in the CMB from the PLANCK survey [11]. The global DM abundance, determined from cosmological probes, estimate WIMPs’ interaction cross section with a result $\langle \sigma_{\chi\nu} \rangle \sim 10^{-5} \text{ cm}^3/\text{s}$ [12], very similar to the weak interaction cross section. This suggests a possible interaction via the weak force, but there are no other dark matter observations that support this assumption. If there is a new stable particle at the electroweak scale, it is a possible DM candidate.

2.2 General Properties and Candidates of Dark Matter

Despite the fact that dark matter exists, it is still unknown whether dark matter is made up of particles or interacts with baryonic matter through forces beyond gravity. However, its gravitational effects and numerical simulations somewhat constrain the requirements for a DM candidate.

The cosmological observations suggest that the dark matter particles do not interact through electromagnetic or strong nuclear forces. Instead, they primarily interact via gravity, and it is theoretically possible that dark matter could interact weakly with baryons. Additionally, it is “dark” (electrically neutral) and cold, meaning it behaves non-relativistically, which better reproduces the dynamics of large-scale structure formation observed today. Finally, it requires temporal stability with a lifetime comparable to the age of the universe; otherwise, it would have decayed. It must also have the correct relic abundance.

Many potential candidates have been proposed. The non-particle theories suggest that dark matter could consist of primordial black holes (PBHs) or arise from modifications to the theory of gravity. The Bullet Cluster remains the strongest argument against modified gravity theories, as require that the centers of gravity decouple from the centers of mass. The particle dark matter theories explain all observed phenomena by introducing a new massive particle that constitutes the dark matter energy density. However, no information about its mass or interaction cross-section is available, leaving a broad parameter space to explore. Although somewhat weakened by the lack of SUSY particles at the LHC, this hypothesis remains of considerable interest due to its experimental feasibility and justifiable cost-benefit ratio. Axions and WIMPs — or more generally, axion-like and WIMP-like particles — are two leading candidates in the direct detection of dark matter.

The only viable SM candidate, the neutrino, is excluded as a dark matter particle due to its too-small mass, which would make it move at relativistic speeds at the time of decoupling and later, dubbed hot dark matter. However, its hypothetical right-handed partner, the sterile neutrino, could be a viable dark matter candidate with a mass range of about keV. Its interaction cross-section would be very low because of its ignorance of the mediators of weak nuclear force, which makes it detectable only indirectly as missing mass in a neutrino spectrum.

Axions were postulated to solve the strong CP problem and are theorized as very light, neutral, non-thermally produced pseudo-scalar bosons. Most searches focus on the meV to μeV mass range, testing the predicted coupling with the photon field in the presence of a strong magnetic field via the Primakov effect. Another wave-like dark matter candidate is the dark photon, a predicted boson that could be a massive mediator between dark sector particles and SM particles. It could couple weakly to the EM field through a coupling parameter ε , making it detectable. However, this coupling must be introduced per hand in the Lagrangian, rather than predicted by an underlying mechanism.

Many theories for new physics at the electroweak scale (e.g., SUSY with the neutralino) introduce a stable, weakly interacting neutral particle with mass $M_\chi \sim 10 - 10^3 \text{ GeV}$, referred to as a WIMP χ . A production mechanism for this particle would have occurred in the early universe, above a certain energy density, and also annihilation mechanisms. This model gained significant attention when it was proposed that a DM particle with a mass on the order of 100 GeV, interacting via the weak nuclear force, could explain the observed dark matter abundance. This convincing and elegant model led to the term “WIMP miracle”.

2.3 WIMP-Nucleus Interactions

Assuming the ¹Standard Halo Model (SHM), a WIMP flux is expected in terrestrial detectors due to the Solar System's relative motion inside the Milky Way, with an average velocity of hundreds of km/s. Since WIMPs do not interact electromagnetically (weak force) and are not relativistic, their detection is typically modeled through elastic nuclear scattering as the primary interaction channel, producing nuclear recoils with energies of

$$E_R = \frac{4M_N M_\chi}{(M_N + M_\chi)^2} \frac{(1 - \cos\theta)}{2} E_\chi, \quad (2)$$

with θ the scattering angle and M_N, χ the masses of the target nucleus and the WIMP, respectively. Here, the kinetic energy of the nuclear recoil E_R is a *kinematic* fraction of the WIMP's most probable kinetic energy. For Ar nuclei, the main component in the DS-20k setup, and intermediate-mass WIMPs, this results in recoil energies on the order of keV.

Then, a predicted scattering rate of DM particles can be derived in the detector's sensitive volume. This event rate depends on a set of astrophysical parameters, with the scattering cross section and DM mass as free parameters of the theory. Thus, it is given by

$$\frac{dR(E_R, t)}{dE_R} = \frac{\rho_\chi}{M_\chi M_N} \int_{v_{min}}^{v_{esc}} v f(\vec{v} + \vec{v}_E(t)) \frac{d\sigma(E_R, v)}{dE_R} d^3v \otimes G(E_R) \quad (3)$$

where R is the scattering rate per unit mass, σ is the WIMP-nucleus cross section, and the convolution \otimes with the function $G(E_R)$ symbolically accounts for experimental features such as resolution, ²nuclear quenching, and acceptance in the region of interest (ROI). The DM halo is characterized by the normalized velocity distribution $f(\vec{v} + \vec{v}_E(t))$ in the Earth's frame and the local density ρ_χ . The WIMP speed is defined in the detector's rest frame, with v_{min} the minimum detectable velocity (set by the experimental energy threshold) and v_{esc} the Milky Way escape velocity, taken as the cut-off for the Maxwellian velocity distribution.

The unknown WIMP-nucleus interaction can be separated into two different contributions, spin-dependent (SD) and spin-independent (SI). The SD interaction couples χ to the spin of the unpaired nucleons, while the SI interaction involves the entire nucleus. Consequently, the time-integrated differential cross section is expressed as

$$\frac{d\sigma(E_R, v)}{dE_R} = \frac{M_N}{2v^2\mu^2} \left[\sigma_0^{SI} F_{SI}^2(E_R) + \sigma_0^{SD} F_{SD}^2(E_R) \right], \quad (4)$$

where μ is the reduced mass of the WIMP-nucleus system, $F_{SI,SD}(E_R)$ are the nuclear form factors, and σ_0 the cross-sections in the limit of zero momentum transfer. The SD cross-section σ_{SD} is approximately proportional to $J(J+1)$, where J is the nuclear spin, while the SI cross-section σ_{SI} increases significantly with the mass of the target nuclei, being proportional to the square mass number A^2 . This indicates the need for experiments using different targets, such as argon (Ar) and xenon (Xe), which complement each other in sensitivity.

¹This simple and sufficiently satisfactory model for dark matter distribution in galaxies assumes an isotropic, isothermal sphere halo of WIMP-DM with a density profile of $\rho(r) \propto r^{-2}$ and a Maxwellian velocity distribution.

²The nuclear and electronic recoil energy scales differ due to distinct energy-loss mechanisms, and their ratio is crucial for accurate interpretation. Thus, results are usually reported in electron-equivalent energy (e.g. keV_{ee}), with the quenching factor measured through neutron calibration experiments.

The equation 3 in the SI case can be integrated over the experimental energy window and expressed as a function of $\sigma_{SI}(M_\chi)$. An experimental limit, e.g. the absence of events at 90% C.L., typically looks like an asymmetric hyperbole branch: the left branch represents the experimental threshold, while the right branch corresponds to the loss of sensitivity due to the reduced density of targets for heavier DM masses. The maximum experimental sensitivity is typically achieved for $M_\chi \simeq M_N$, corresponding to the minimum of the curve.

The scattering rate for a weak interaction scales with the measurement time and the target mass, whose product is known as the exposure. Given the expected WIMP cross sections, ranging from 10^{-50} to 10^{-40} cm², very large detection volumes are required. Therefore, direct WIMP search experiments demand scalable technology and a very low-background setup to detect these small (keV-scale and below) and rare (fewer than ~ 1 event/(kg yr)) events. Noble liquid detectors in the dual-phase TPC layout are the most promising option for detecting potential WIMP signals, as they meet all these requirements.

For a complete version, Earth's motion through the Milky Way induces a seasonal variation of the total event rate and a forward-backward asymmetry in a directional signal. These effects also provide a powerful dark matter signature.

2.4 Current Status

The energy deposited by particle interactions in the target medium - whether from nuclear or electron recoils - can generate three measurable signals: ionization (charge carriers), scintillation (photons), or lattice vibrations (phonons). Experiments often combine these observables to improve particle identification and background rejection.

To determine the nature of DM and test the favored parameter space of DM models, a wide range of direct detection experiments, using different technologies, is underway. These include cryogenic bolometers with scintillation or ionization (CRESST-III, SuperCDMS), scintillator crystals (DAMA/LIBRA, ANAIS), semiconductor ionization detectors (DAMIC with CCD sensors), bubble chambers (PICO), point-contact germanium detectors (MALBEK), and noble liquid detectors (xenon: PandaX-4T; argon: DEAP-3600, DarkSide-50). The common goal is to achieve low energy thresholds and operate at ultra-low background levels to achieve the highest possible sensitivity.

The strongest results in the low-mass (< 10 GeV) WIMPs region are currently obtained by cryogenic bolometers, thanks to their extremely low energy thresholds. In the classical WIMP mass range, massive LAr (DarkSide-20k) and LXe TPCs (XENONnT, LZ) dominate, as they can be scaled to ton-scale target masses, and therefore high exposure can be collected. Furthermore, heavy targets increase the expected scattering rate for high DM masses. Their results approach the neutrino floor, an irreducible background from coherent elastic scattering of solar and atmospheric neutrinos that produces nuclear recoils indistinguishable from those caused by WIMPs. This experimental limitation could, in principle, be addressed by future directional detectors, which exploit the directionality of nuclear recoils.

The motivation for direct WIMP searches remains strong, particularly for high masses (above a few hundred GeV), which lie beyond the LHC reach, as well as for the region of low cross-sections (10^{-45} cm² to 10^{-47} cm²) associated with Higgs-mediated scattering. Due to the different masses of the target nuclei and experimental thresholds, xenon and argon detectors are more sensitive to the lower and higher sides of WIMP mass range. Figure 1 shows that

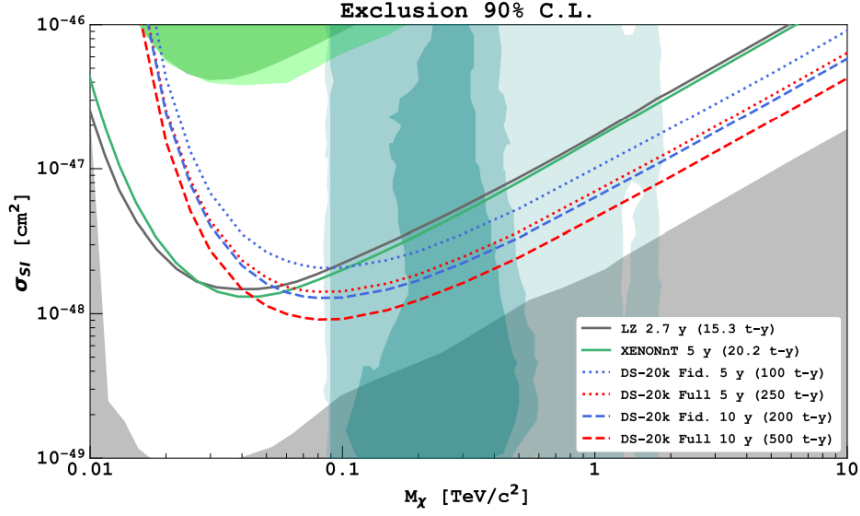


Figure 1: Sensitivity of DarkSide-20k to spin-independent WIMPs for different lengths of runs, with the full exposure and fiducial cuts applied, compared to LZ (2.7 yr run, 15.3 t yr exposure) and XENONnT (5 yr run, 20.2 t yr exposure). The lower region represents the *neutrino fog*, where the backgrounds from neutrinos begin to dominate the event rates, and the turquoise filled contours indicate the parameter space favored by the pMSSM11 model [13].

the DarkSide-20k experiment will probe spin-independent WIMP-nucleon interactions down to 10^{-48} for a 0.1 TeV WIMP, with a confidence level of 90 %. For WIMPs with masses $M_\chi \gtrsim 0.1$ TeV, DarkSide-20k provides better exclusion limits than xenon-based experiments (LZ, XENONnT), covering a region favored by the pMSSM11 model (at $1 - 3\sigma$ C.L.), while for WIMPs with $M_\chi \lesssim 0.1$ TeV the projected exclusion sensitivities remain competitive.

2.4.1 Xe vs Ar

The TPC consists of a liquid-filled detection volume immersed in a uniform electric field that drifts ionization electrons toward the top. This technology, using an ultra-pure noble liquid as the target material, are very succesful in exploring the WIMP ROI — within the ranges specified above — by detecting nuclear recoils. Such detectors can operate in single-phase (liquid) or dual-phase (liquid and gas) configurations. Since charge detection is more efficient in gas, while achieving a large target mass is easier in liquid, a dual-phase TPC is optimal for these searches.

Among the noble elements, xenon and argon are promising candidates due to their advantageous properties and their sensitivity exclusively to spin-independent interactions. Their high scintillation yield allows for very low detection thresholds for particle interactions, down to the keV range, and they can be easily ionized. In liquid state, these elements are used to build massive, dense and compact DM targets which have already exceeded the ton-scale. They can be easily purified, which implies a high electron mobility and long drift distance ($D > 1$ m).

The processes for liquid argon and xenon are essentially the same, except for the wavelengths and lifetimes of the produced light. Xenon has two similar decay constants (4 ns and 22 ns), while the decay constants of argon differ significantly (1.6 μ s and 7 ns), allowing efficient pulse shape discrimination (PSD). This property is a key feature of argon, providing

a unique tool for rejecting electron recoil (ER) backgrounds. Furthermore, argon is much cheaper and available in large quantity, allowing for the construction of even larger detectors. Its low production cost is due to its abundance in the Earth’s atmosphere. In the xenon case, it is evident a gradual difficulty in the scaling process. However, unlike xenon, which is intrinsically radiopure, the natural argon is contaminated by cosmogenic radioactive isotope ^{39}Ar , a long-lived beta emitter that constitutes a non-negligible source of ER background events. This issue can be strongly mitigated by extracting argon from underground wells, where it has been isolated from the atmosphere and depleted of ^{39}Ar .

For these reasons, the Global Argon Dark Matter Collaboration (GADMC) — bringing together members from ArDM, DarkSide-50, DEAP-3600, and MiniCLEAN, the four world-leading argon dark matter projects — was established in 2017 to pursue a sequence of future argon-based experiments, beginning with DarkSide-20k. A subsequent objective is the Argo experiment, a detector with an active volume of 400 t (300 t fiducial mass) of low-radioactivity argon, which explore the experimentally accessible parameter space for WIMPs in a wide mass-range, down to the *neutrino fog*.

3 The DarkSide-20k Experiment

The DarkSide-20k experiment, currently under construction and expected to begin data-taking in 2027, is mainly designed to perform an instrumental background-free search for high-mass (> 10 GeV) WIMPs, with fewer than 0.1 background events in a 200 t yr exposure. The particle detection relies on the combined measurement of scintillation light (S1) and ionization charge (S2). Based on the successful experience of DarkSide-50 (DS-50), it will utilize the same dual-phase LAr TPC technology, but with a fiducial mass of 20 t instead of 20 kg, while significantly improving the radiopurity of its components.

To manage this scale-up, technological upgrades are needed, such as the use of Silicon Photo-Multipliers (SiPMs), and tested in intermediary prototypes like Proto-0 and Proto-1t at CERN. The increased detector volume also introduces challenges, as the pile-up events due to the longer drift time of ionization electrons in the TPC. This chapter describes the DS-20k design, typical background sources, expected signals, and pile-up problem in multi-ton TPCs.

3.1 Background Events and Mitigation Strategies

Direct detection experiments aim to either detect WIMPs (with 5σ discovery) or exclude the corresponding energy-interaction range. An optimal detector must minimize both internal and external radioactive backgrounds, while remaining sensitive to potential dark matter signals. Successfully detecting a WIMP requires not only high sensitivity, but also the ability to suppress and discriminate background events that could mimic the expected signal.

Depending on the nature of the incident particle, scattering can occur with the nuclei (nuclear recoil, NR) or the electrons (electron recoil, ER) of the target. As discussed in 2.3, WIMPs are expected to interact primarily with nuclei, producing elastic NRs. In liquid argon, ER backgrounds can be suppressed by several orders of magnitude using PSD techniques. The shape of the S1 signal, as well as the ratio between S1 and S2, are used for particle identification to distinguish potential signals (i.e. single-scattering NR inside the fiducial volume) from backgrounds such as heavily ionizing particles (mainly α 's) and ER events (β and γ radiation).

Neutron-induced NR events are one of the most significant background in these searches, as their signature can mimic WIMP-like signals. However, they have different energy spectra and multiple-scattering. Radiogenic neutrons arise from ³(α , n) and spontaneous fission reactions, while cosmogenic neutrons are produced in cosmic-ray muon showers through spallation reactions. Mitigating this background involves the selection of materials with low levels of radioactive contamination, comprehensive shielding of the detector using both active and passive veto systems, and the location of experiments in deep underground laboratories to minimize exposure to external radiation. Techniques such as fiducialization, which involves selecting a clean inner volume to reduce backgrounds originating at the detector surface, play a fundamental role in DM data analysis. In addition to cosmic and environmental backgrounds, instrumental effects and spurious signals can also mimic real events, requiring careful filtering and calibration procedures.

³The α particles are produced by the ²³⁸U and ²³²Th decay chains, which account for 6 and 8 α -decays, respectively. Each of these decays may induce an (α , n) reaction in the medium. These elements are present in trace amounts in all materials.

3.2 The DS-20k Detector

The DS-20k detector will be located at a depth of 3400 m.w.e. in Hall C of the INFN Gran Sasso National Laboratory (LNGS) in Italy, to cancel the cosmic rate induced background. Like its predecessor, DS-50, its structure resembles a Matriochka, with three main volumes: the TPC detector, the inner (neutron) and outer (muon) vetoes, and the membrane cryostat.

The inner detector consists of an ultra-pure sealed acrylic TPC filled with a 50 t (20 t) active (fiducial) mass of low-radioactivity argon sourced from underground (UAr). The DS-20k TPC is shaped like an octagonal prism, with a vertical drift length of 348 cm and a diameter of 350 cm. The sides of the TPC are covered by reflectors and wavelength shifters (TetraPhenyl Butadiene, TPB) to convert LAr scintillation light (at 128 nm) into visible wavelength (at 420 nm) detectable at high efficiency. The light signals are then redirected to the top and bottom readout planes, which are equipped with 21 m² cryogenic SiPMs, ensuring the optimal collection of both scintillation and ionization-induced photons.

The active volume is immersed in a uniform electric drift field of 200 V/cm, generated by applying a 73.4 kV potential between the cathode and anode planes, both made of transparent acrylic (PMMA) coated with a Clevios conductive polymer. The lateral walls are also coated with Clevios electrodes, behind the reflector panels, to ensure uniformity of the drift field. A steel wire grid with 3 mm spacing, placed 1 cm below the liquid surface, generates the strong electric field required for the extraction of electrons in the 7 mm gas pocket, allowing the development of the S2 electroluminescence signal. The grid operates at 3.8 kV, which corresponds to an extraction field of 2.8 kV/cm and an electroluminescence field of 4.2 kV/cm.

To suppress the background produced by external radiation, the multi-ton dual-phase TPC at the detector's core is surrounded by multiple layers of shielding and active veto systems. The inner veto is also filled with UAr (32 tonnes), enclosed in a gadolinium-loaded (1%) acrylic shell to enhance neutron thermalization and capture. This inner veto is instrumented with 5 m² of cryogenic SiPMs, capable of detecting single photoelectrons with high spatial and temporal resolution and providing a light yield of about 2 photoelectrons per keV. The neutron background is efficiently suppressed if coincident energy deposits are observed in both the TPC and the surrounding UAr.

Both the TPC and the inner veto are housed within a titanium cryostat containing a total of 99 tonnes of underground argon. This assembly is enclosed in a larger ProtoDUNE-like membrane cryostat filled with more than 650 tonnes of atmospheric argon (AAr), which acts as both a passive shield against external radiation and an active muon veto. Independent cryogenic purification systems are used for the UAr and AAr volumes to maintain the required levels of purity.

The light detection system in the TPC comprises two planes of SiPM-based Photodetector Modules (PDMs), covering its top and bottom inner faces. The choice of SiPMs over traditional photo-multipliers (PMTs) is motivated by their advantages: the higher photo-detection efficiency (typically exceeding 50% at 420 nm), the superior single-electron resolution, the lower operating bias voltage (< 100 V), and the smaller amount of required material, making them potentially extremely radio-pure. The PDMs, which include the front-end electronics, are arranged in 2090 readout channels, with the S1 yield greater than 10 phe/keV (photons per keV of deposited energy) and the S2 yield greater than 20 PE/e⁻ (photoelectrons per ionization electron) extracted in the gas pocket. The front-end boards digitize and amplify the signals and are mounted parallel to the tiles, with optical transmitters driving the signals.

3.3 Light Production in Liquid Argon

Particle scatters within the liquid argon medium can produce heat (undetected), ionization and excitation of the argon atoms. The excited state (Ar^*) forms excited dimer states or excimers (Ar_2^*) by combining with a ground-state argon atom (Ar). The direct de-excitation of the Ar atoms is slower and suppressed compared to the formation of these excimers (< 1 ns). In parallel, ionized argon atoms (Ar^+) form molecular ions (Ar_2^+) with neutral argon atoms and recombine with free electrons, resulting in the same excited di-argon states produced by excitation. In this case, the formation of molecular ions, which occurs on a timescale of the order of picoseconds, dominates over direct electron-atom recombination.

In both processes of light emission in LAr, the Ar_2^* excimers emit scintillation light (called primary scintillation, S1) at 128 nm in the vacuum ultraviolet (VUV) band when de-exciting and dissociating into two ground-state Ar atoms. The de-excitation occurs with different radiative decay constants depending on the spin state of the excimer Ar_2^* , which can exist in either singlet ($^1\Sigma_u^+$) or triplet ($^3\Sigma_u^+$) states. Singlet transitions for Ar have a lifetime of nanoseconds, while direct triplet transitions to the ground state ($^1\Sigma_g^+$) are forbidden. The relative populations of singlet and triplet states, and thus the scintillation pulse shape, differ between electronic and nuclear recoils. Conveniently, liquid argon does not absorb its own scintillation light, allowing it to be measured. Only impurities can re-absorb VUV light and capture electrons.

Therefore, for each primary interaction in the liquid target, two signals are used: a prompt scintillation signal (S1), produced in the liquid, followed by a delayed electroluminescence signal (S2), generated by accelerated ionization electrons in the gas pocket. S1 is detected by both the top and bottom SiPM arrays of the detector, while S2 is primarily detected by the top light-readout devices. The S2 signal is more intense than S1 and is proportional to the initial ionization, providing a measure of the charge through its electroluminescence photons. S1 and S2 signals are typically correlated due to ion recombination.

3.4 The Pile-up Problem

The detector provides full 3D event reconstruction. The (x, y) coordinates of the interaction are determined from the light distribution recorded by the top photosensor array, while the z -coordinate is inferred with sub-millimeter precision from the time delay between the prompt S1 and delayed S2 signals, using the known⁴ electron drift velocity and drift length of the TPC.

These detectors expand in size as the drift time increases. The longer drift time of the electrons increases the probability of pile-up, a phenomenon in which signals from different events are recorded simultaneously, which can cause multiple ionization signals to overlap. This scenario introduces ambiguity in associating events, potentially leading to misinterpretations in accurate position reconstruction. The rejection of such pile-up or accidental coincidences would result in a significant loss of lifetime for DS-20k. Since pile-up defines the dead time between the acquisition of different pulses, it directly impacts the fraction of signal that may be lost as their S1 and S2 are not matched together (cluster with only one pulse).

WIMPs are expected to scatter only once in the LAr volume of the TPC due to their extremely low interaction probability. Such interactions are reconstructed as single-S1 and single-S2 events, with energies on the order of keV. Consequently, multi-scatter events (pro-

⁴The free electrons in a uniform field through a dense medium quickly reach a constant drift velocity.

ducing more than one S2) are rejected, as they do not correspond to the expected WIMP signature. Pulses are required to be isolated from any other S2 pulse preceding or following by more than the maximum electron drift time in the DS-20k TPC (3.5 ms).

If the z -coordinate (vertical coordinate) can be reconstructed from the S1 light pattern, a unique association between S1 and S2 events becomes possible when events are spatially separated. This creates a certain time window in which the S2 corresponding to a specific S1 is expected. Thus, accurate S1-based position reconstruction becomes pivotal, alleviating the constraints on the maximum event rate that can be handled and the requirements on the event rate and material contamination. Figure 2 illustrates a simple case, while more complex scenarios may involve multiple S2 signals for a single S1. In this example, two distinguished events are recorded within the same data-taking gate, and the correct S1–S2 association ensures that the cluster is preserved.

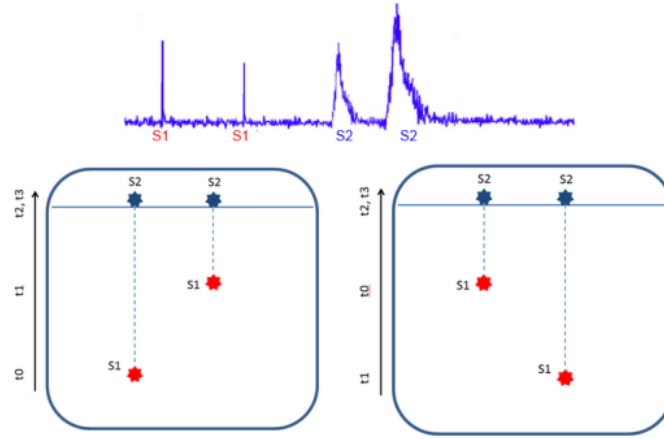


Figure 2: Scheme for the simple case of two independent events simultaneously recorded in a same drift time window. Each event produces an S2 signal. If the S2 pulses deposits are very close to each other, they may appear as one indistinguishable pulse. It is assumed that two close S2 pulses can be distinguished if they are separated in time by more than $2 \mu\text{s}$ (2 mm along the drift direction), as achieved in DS-50.

4 S1 z -Reconstruction

In DarkSide-20k, the expected event rate is about 120 Hz, and the maximum electron drift time is 3.5 ms [14]. This would result in approximately 42% pile-up, leading to the loss of a significant share of exposure. A solution would be to develop an algorithm for z -reconstruction of the S1 pulses, which predicts the vertical coordinate and associated uncertainty of all interaction vertices, thereby removing the ambiguity introduced by pile-up.

The S1 z -reconstruction is here based on the distribution of the channel occupancy, using supervised learning with deep neural networks to achieve high accuracy and computational efficiency compared to classical methods, which are more established and well studied.

This chapter is structured as follows. In Section 4.1, the synthetic data of realistic recoil events used to train and validate the proposed models is described; in Section 4.2, the training process and model architectures are summarized; and in Section 4.3, the performance evaluation on a test set is reported. Finally, a comparison of the two representations is provided.

4.1 Used data

The data used for the S1-only analysis were produced with G4DS [15], a Geant4-based Monte Carlo simulation framework that implements a detailed geometry of the DarkSide-20k detector and includes realistic optical models for scintillation light production and propagation. As for the expected dark matter interactions, the simulated dataset includes interactions generated uniformly across the entire TPC, with the number of events increasing with radial distance R . At the same time, events at fixed positions have been simulated to test reconstruction performance.

Data sets of 10^4 electron events at different energies of 2, 8, 20, and 30 keV are simulated for the study. The data is balanced across the height of the TPC, in order to prevent the network from adapting to a specific case and producing a biased model. Each SiPM array consists of 1045 channels arranged in a 35×35 grid, filled with both light and position information for each channel. Consequently, each simulated event is represented by an image of the light pattern in terms of number of photoelectrons in each (X,Y) PDM (see Figure 3).

In Figure 3, certain S1-light patterns can be observed. Depending on the S1 position, the top and bottom planes of the TPC do not receive the same amount of light. Light arrives with a large solid angle due to the TPC height and after multiple scattering. Only scattering is selected, and reflections occur on the walls of the TPC and in the gas pocket. The illumination is not localized, and additional information does not benefit the reconstruction.

In a given plane, more photoelectrons are observed because of an asymmetric dispersion between the top and bottom planes. On the z coordinate, an event in the center of the detector produces less light on both detection planes than an event near the top or bottom. When the event occurs in z near the top plane, its 2D variance is larger on the top plane and smaller on the bottom. The opposite happens when the true position of an input event is near the bottom plane. In addition, signals at 8 keV are small and hence it is hard to find relevant features in the light pattern. The signals are fainter in the lower energy range due to a smaller signal-to-noise ratio (SNR). Therefore, we focus on the S1-based z -reconstruction using 30 keV events.

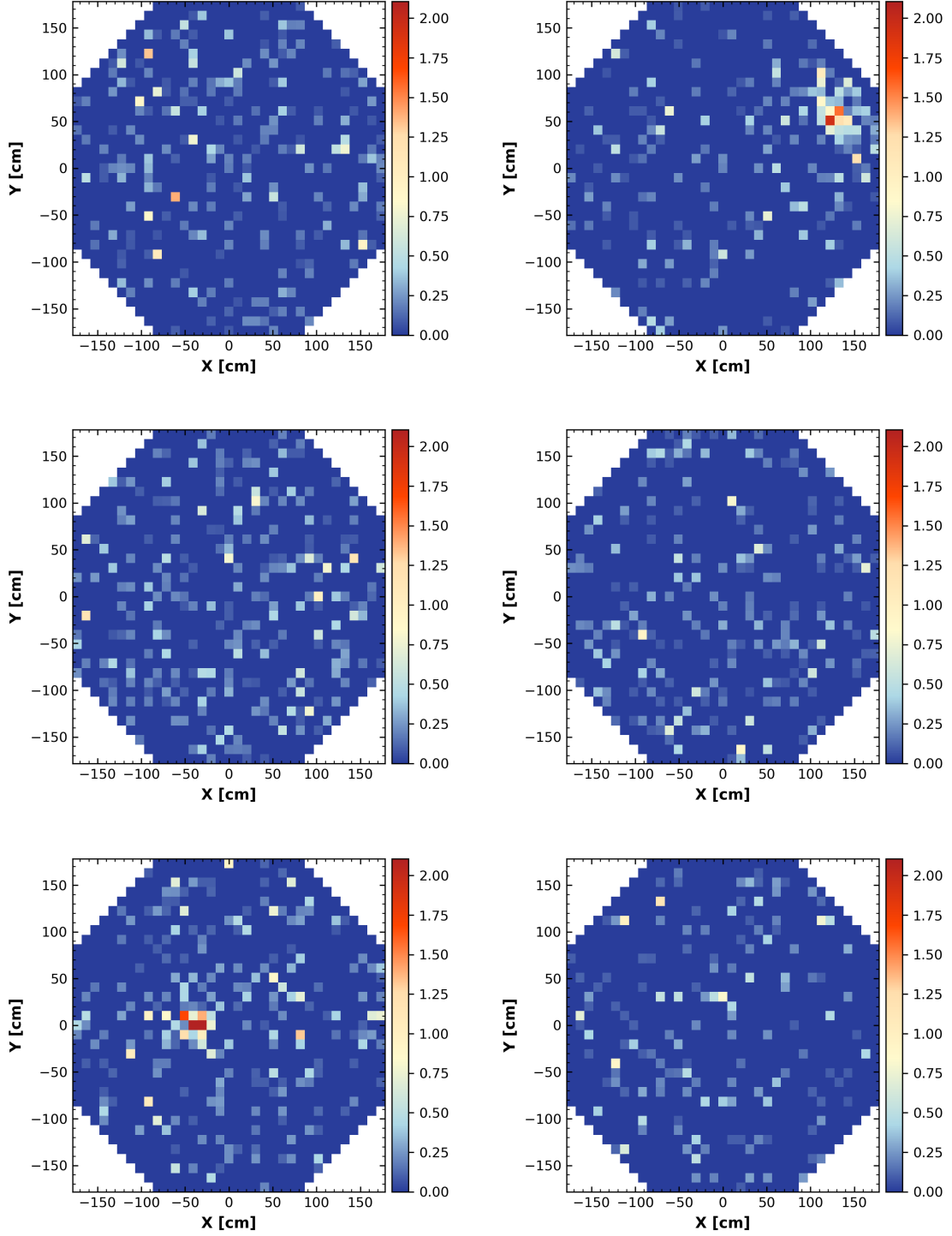


Figure 3: Example of light patterns detected for configurations with z high, z medium, and z low (respectively for XYZ at 133, 55, 162 cm; -76, -69, 25 cm and -35, 2, -172 cm) in the bottom (left) and top (right) planes for 30 keV events. The color scale represents the number of photoelectrons detected in each light channel, treated as individual detectors in the dataset. Color bars are scaled from 0 to the 0.90 quantile of the maximum intensity distribution across events. Saturated pixels are clearly visible, while missing data are encoded as null values.

4.2 Neural Networks and Deep Learning

Deep Learning (DL), a subset of Machine Learning (ML), utilizes Neural Networks (NN) to learn from labeled data and predict outcomes on unseen inputs. In Particle Physics, NNs hold the key to interpreting intricate patterns of interaction with large errors in the challenges posed by pile-up. Position reconstruction is categorized as a regression problem in ML, wherein continuous labels, in the form of coordinates, are predicted.

Neural networks are powerful general-purpose function approximators capable of learning complex and nonlinear relationships in high-dimensional data. They exploit correlations and extract salient features for decision-making. Inspired by the structure and function of the brain, these algorithms consist of simple interconnected processing units, or neurons, arranged in a layered structure. Such multilayer networks are often called “deep networks”, especially when they include more than a few layers.

The main advantage of deep learning is its versatility and composability, allowing the development of purpose-built architectures that define the shape and configuration of layers in a NN. Very deep neural network models process data within these architectures but often end up memorizing training data instead of learning the underlying relationships. This issue, known as overfitting, must be avoided. A model that performs well on training data but generalizes poorly to unseen data is ineffective and prone to producing inaccurate predictions.

Architectures such as multilayer perceptrons (MLPs) and convolutional neural networks (CNNs), each carrying unique attributes and trade-offs, will be covered. All models have been implemented using TensorFlow and Keras, a high-level API designed to work with NNs, facilitating seamless execution on both CPUs and GPUs. During training, hyperparameters such as learning rate, batch size, and dropout will be explored, along with how to optimize them for better performance.

4.2.1 Multilayer Perceptron

The model is associated with a directed acyclic graph, where each node indicates a scalar variable. For any neuron, its value is obtained as follows:

$$z_j^{(n+1)} = \sum_k w_{jk}^{(n+1)} y_k^{(n)} + b_j^{(n+1)}, \quad (5)$$

$$y_j^{(n+1)} = f\left(z_j^{(n+1)}\right). \quad (6)$$

First, an affine transformation is applied (Eq. 5), where the coefficients w are the “weights”, and the constant offset b is the “bias”. These define how neuron k in layer n will affect neuron j in layer $n + 1$, and together form the network parameters θ . They will be updated during training. Then, a nonlinear function f is applied (Eq. 6) to produce the activation.

The layers consist of units that act in parallel, each representing a vector-to-scalar function. Typically, neurons in such networks are organized into three parts: the input layer, an arbitrary number of hidden layers, and the output layer with predictions. The input layer passes a specific input vector \vec{x} , with the same number of components as variables in the data. The neurons in the hidden layers apply an activation function f , which is usually fixed, while in the output layer the activation function depends on the task. In numerical regression, a

linear function is usually used, while in classification problems the sigmoid function or its generalization, softmax, for multiple categories, are used.

In the classical approach, solving a task involves writing a sequence of instructions. In contrast, the machine learning approach rephrases the task as a minimization problem:

$$\theta^* = \operatorname{argmin}_{\theta} \mathbb{E}_{\vec{x} \sim p(\vec{x})} [\mathcal{L}(F_{\theta}(\vec{x}), \vec{x})], \quad (7)$$

where the optimal parameters of the model in a NN are obtained by minimizing the expected value of a loss function over the data distribution. This function measures the deviation (error) between the forward pass output and true labels, reflecting the quality of the model's performance. The choice of loss function also depends on the problem type, with mean squared error (MSE) commonly used for regression tasks and cross-entropy for classification. Notably, these loss functions are similar to those used in other parametric models, such as linear models.

Once the cost function has been defined, the parameters θ in the high-dimensional space are fitted using backpropagation algorithms and gradient descent, known as optimizers. These facilitate and accelerate convergence of the method to a global minimum (or its closest approximation) in the fewest possible iterations. For feedforward NNs, it is important to initialize all weights to small random values, and the biases may be initialized to zero or to small positive values. There's some amount of stochasticity in the training. The partial derivatives of the cost function with respect to each component of θ are computed starting from the output layer backward through the network to the first hidden layer. This implementation is mathematically based on the chain rule of differential calculus.

Once all derivatives have been evaluated, the parameters are updated by subtracting the gradient from the current value:

$$\theta^{(n)} \leftarrow \theta^{(n)} - \eta \nabla_{\theta^{(n)}} \mathcal{L}(\theta) \quad (8)$$

where η is the learning rate and is related to the speed at which the training approaches the minimum of the cost function. A higher learning rate can make the training process faster by taking larger steps toward a minimum. Still, it can also miss a minimum entirely. A lower learning rate makes the training process slower, but it can also make the network more accurate. Currently, there are more effective optimizers, such as AdaBoost or Adam. These aim to adjust the direction of the gradient and optimize the learning rate.

Each time the network processes all training data, an epoch is completed. The cost function is ideally an average over all inputs, but this is too expensive to compute at every step, and the entire training data often cannot fit into the computer memory. This is addressed by consecutively averaging over subsets of training samples for each step, called batch size. Small values offer greater variability in the gradients and faster computation.

The values that define the network's structure are called hyperparameters. They govern the training of learnable parameters and can be divided into the categories of architecture, optimization, and regularization. Architectural hyperparameters include the number of layers or their width; optimization contains batch size and learning rate; and regularization involves methods like dropout, which randomly switches off learnable parameters during training to prevent overfitting. In dense networks, dropout is the main regularization layer. Techniques such as callbacks help monitor overfitting and the validation set is used to evaluate model performance during training.

It is often difficult to predict the effect of changing a hyperparameter without testing it, which leads to extensive trial and error and a thorough exploration of the hyperparameter space. Methods for hyperparameter tuning, such as grid search and Bayesian optimization, can efficiently explore this space and find the best combination for a specific task. However, although these methods can be automated, they are computationally expensive and require significant time and resources. Optimizing the network involves finding the optimal parameters and hyperparameters for a given problem.

4.2.2 Convolutional Neural Networks

Convolutional neural networks (CNN) are neural networks based on the convolution operation. They are well-suited for processing grid-like data where spatial relationships are essential, and the main goal is to identify features in images and detect patterns.

In a CNN, the neurons in the hidden layers are not all connected to each other but are organized in small receptive fields that process only a part of the input at a time. These receptive fields can move across the entire image, allowing the network to account for locality (correlation of nearby pixels) and translation invariance. Mathematically, this is represented by a convolution, which applies two functions to each other and works like a sliding window.

In the 1D case:

$$w_{ij}^{(n+1,n)} = w^{(n+1,n)}(i - j), \quad (9)$$

where the function $w^{(n+1,n)}(i - j)$ is called the “kernel” or the “filter”. It is set to zero for $|i - j| > d$, so the weights depend only on the distance. Furthermore, CNNs use “weight sharing”, which means that all neurons within a receptive field use the same weights. This leads to a huge reduction in the number of weights that need to be stored and updated during training. Instead of M^2 weights (if both layers have M neurons), there are only $2d + 1$, which do not depend on the size of the layer. The standard network layout discussed above is termed “densely connected” layers, in contrast to CNNs, which have a sparse weight matrix.

In 2D, the kernel depends on $i_x - j_x$ and $i_y - j_y$, because each neuron sits at a specific pixel in an image labeled by two discrete coordinates, $i = (i_x, i_y)$. Thus, it is given as a small 2D array of dimensions $(2d + 1) \times (2d + 1)$.

The linear part of the network’s operation is

$$z_i^{(n+1)} = \sum_j w^{(n+1,n)}(i - j) y_j^{(n)} + b^{(n+1)}. \quad (10)$$

Applying these filters is a linear superposition of the original pixel weighted by the kernel values. They can detect abstract features in the data, such as extracting contours or smoothing the initial image. In deep CNNs, task-specific details emerge in higher layers during training. The difference from traditional image processing is not only the use of nonlinear activation functions but, more importantly, that the CNN filters are learned automatically during training.

Often, the data used in a CNN have multiple channels. This requires introducing an extra channel index c , such that each neuron is now labeled (i, c) . Then, the operation is described by:

$$z_{(i,c)}^{(n+1)} = \sum_j w_{cc'}^{(n+1,n)}(i - j) y_{(j,c')}^{(n)} + b_c^{(n+1)}. \quad (11)$$

A typical convolutional layer has two main stages. In the first stage, it acts as a spatial feature extractor that learns properties that describe the data more globally. After each convolution, nonlinear layers using activation functions break the linearity. In the second stage, a pooling layer reduces the spatial dimensions of the feature maps. This decreases the computational complexity of the model and helps prevent overfitting by subsampling the image while preserving essential features. A CNN usually consists of several blocks, as previously described. After the convolution sector, all neurons in all channels are flattened into a single-dimensional array and fed to densely connected layers that combine the extracted features to complete the task.

4.3 Results

4.3.1 Dataset Description

A total of 80k events of 30 keV electrons uniformly distributed in the active volume of DS-20k have been used, ensuring sufficient statistics. Each simulated event contains information about the true interaction position and the deposits of S1 signals, represented by the light patterns recorded in each detection plane of the detector. The simulated dataset contains fully simulated events including SiPM dark current and electronic noise.

The dataset is randomly split into 60k training and 20k test sets using a 75/25 ratio. This split ensures that the network is evaluated on unseen data, helping to detect overfitting. Models are trained with more labeled data to improve prediction accuracy. In a preprocessing step, all samples are min-max normalized to a value range from 0 to 1 to ensure that the network learns light patterns rather than relying on absolute charge values. This transformation reduces computational cost without significant information loss.

4.3.2 Results for 1D input

Before the CNN, other architectures were evaluated, in particular the MLP. For brevity and taking into account that the results of the CNN outperform those of the MLP, only the former will be presented. The higher efficiency of the CNN over the MLP emerges from its ability to exploit the spatial correlation of the light pattern in the images. This topological information is lost when the matrix representation of the images is turned into a flattened 1D vector with 2090 values representing PDM recordings. In any case, the application of the MLP previously to CNN has been extremely useful as learning process.

4.3.3 Results for 2D input

The architecture used here is a 2D CNN with input tensors of shape $35 \times 35 \times 2$, where each channel corresponds to a detection plane. It consists of two convolutional blocks with 32 and 64 filters, kernel size 3 and *same* padding, using max pooling of size 2. This is followed by two feed-forward layers with 32 and 8 neurons. This model use ⁵ReLU activation function in the hidden layers and the output layer is linearly mapped to estimate the z position.

⁵The ReLU (Rectified Linear Unit) function $f(z) = \max\{0, z\}$ keeps only positive neurons. It is an excellent default for hidden units, with efficient gradient computation and a lower risk of training stagnation.

The model is trained using the mean squared error (MSE) as the loss function and runs for up to 100 epochs. Early stopping with a patience of 3 is applied, meaning training stops if the validation performance does not improve for 3 consecutive epochs. Training is completed in approximately 12 epochs using the ⁶Adam optimizer with its default learning rate and a batch size of 32, on an NVIDIA T4 GPU with up to 12 hours of continuous runtime on the free tier of Google Colab.

This problem has a large amount of data and about 10^5 parameters to train. However, the model converges quickly, with the loss decreasing little after the first epoch. The results for one execution are presented in the following figures.

Analyzing the performance (see Figure 4), the model achieves optimal results for events occurring near the top and bottom of the detector. In contrast, performance degrades for events near the center due to the similarity of light patterns recorded by the photosensor array in that region. Central interactions produce greater light diffusion and reflections from the lateral walls, resulting in blurred patterns that hinder accurate reconstruction.

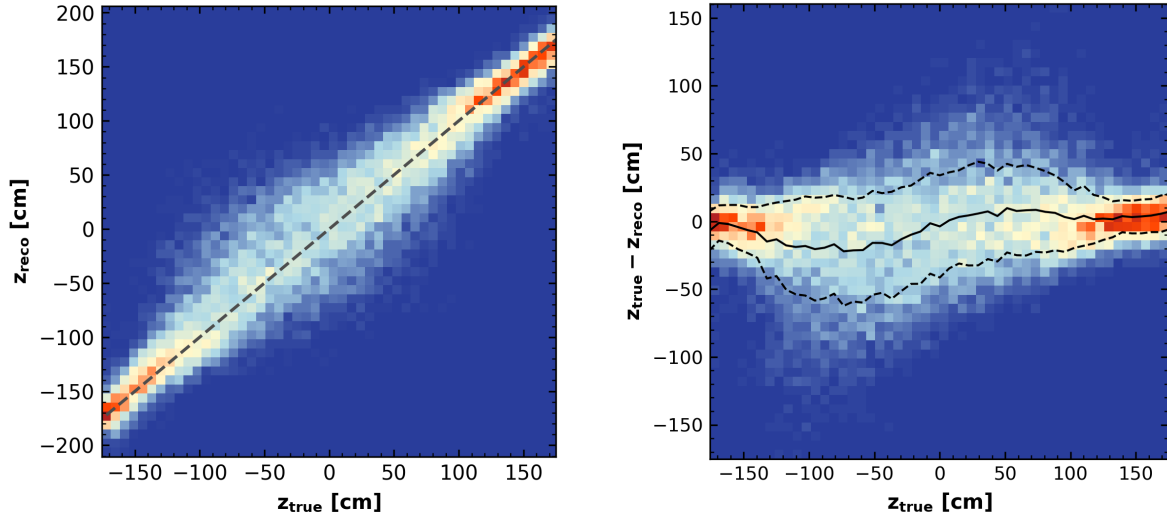


Figure 4: Performance of the model (left figure) and difference between true and reconstructed values (right figure) for the z position. The solid line represents the mean of the distribution, and the dashed lines correspond to the mean \pm RMS (resolution).

The reconstructed error, defined as the true minus reconstructed z position, is not constant. As expected, a bias increase and resolution decrease are observed in the central part of the TPC. Although the precision does not appear to be highly dependent on the (x,y) position (see Figure 5), it is driven by the true z position. This behavior is in agreement with the treatment of the lateral and vertical coordinates independently in the network output.

The distribution is not symmetric with respect to the center of the detector ($z = 0$) due to reflections in the gas pocket. When the true z position is negative and near the center, the model tends to produce negative errors ($z_{\text{true}} < z_{\text{reco}}$), which implies overestimation. The opposite occurs in the positive range, where the model tends to underestimate. Although these are preliminary results, it is proved that it is possible to reconstruct the position through S1 — a significant outcome that is not guaranteed.

⁶The Adam (Adaptive Moment Estimation) optimizer is widely used, combining momentum and adaptive learning rates.

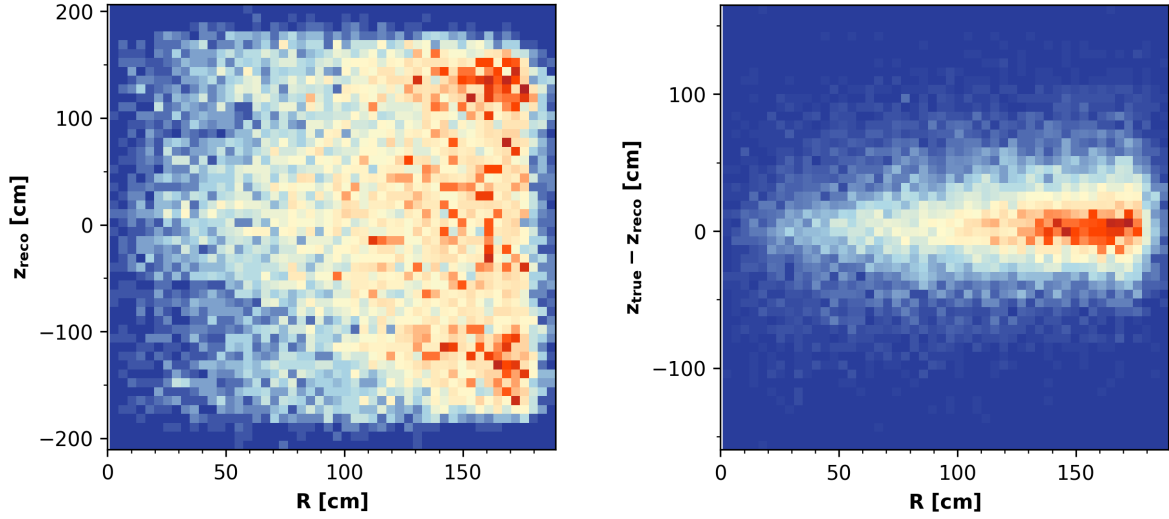


Figure 5: Performance of the model (left figure) and the reconstructed error (right figure) as a function of the radial distance (R) for the x and y coordinates.

In addition, Figure 5 shows that the resolution is parameterized as a function of the position for S1 pulses inside the TPC, in agreement with Figure 4. Due to edge effects in the (x,y) -plane projection, the spatial resolution tends to degrade as R from the center of the detector increases. A fiducialization criterion may improve precision.

In this case, a spatial resolution is obtained in the vertical coordinate σ_z of around 32 cm, with a resolution of -60 to 40 cm in the central part of the detector. Finally, the mean reconstruction error is negative, which implies that the predictions are greater than the true values on average (Figure 6).

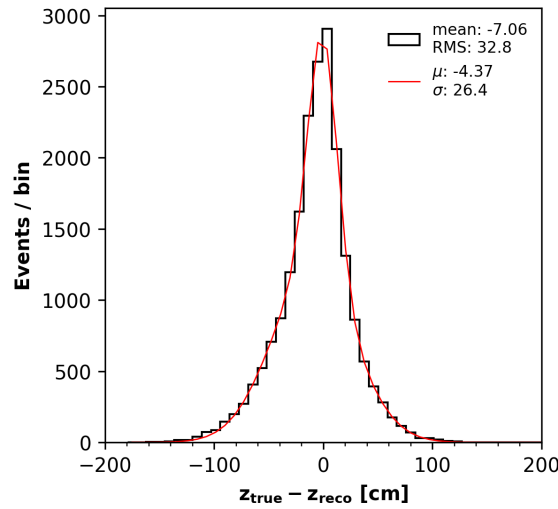


Figure 6: Distribution of the difference between the true and reconstructed z positions. The solid line represents a two-Gaussian fit of the reconstruction error, with contributions from central and near-plane events.

5 Conclusion

The DarkSide Collaboration will construct DarkSide-20k, a dual-phase LAr TPC with an active (fiducial) mass of 50 t (20 t), geared with thousands of silicon photosensor modules, which has two main signals: scintillation in LAr (S1 signal) and electroluminescence in GAr (S2 signal). The DarkSide-20k experiment will be the most advanced and largest liquid argon TPC ever built for DM searches. A successful DS20k detector would represent a crucial milestone toward the realization the next generation of multi-tonne detectors designed to reach a sensitivity very close to the neutrino floor.

Given the large volume and consequently high rate of expected events in the DS-20k detector, the inner TPC will experience a pile-up probability of $\sim 42\%$. The rejection of pile-up events would result in a significant loss of exposure time. A strategy relies on the correct association between scintillation and ionization signals, even in this scenario. An algorithm for z -reconstruction from the S1 light pattern enables a unique association between S1 and S2 events when events are spatially separated.

The integration of Deep Learning in Particle Physics proves crucial for refining algorithms in position reconstruction within dual-phase LAr TPCs of ever-growing size for DM searches. For that, two different NN architectures, each carrying unique attributes and trade-off, are developed to reconstruct the scintillation signal position with a precision. While multilayer perceptron (MLP) and CCN1d models are effective in certain contexts, they use information from the entire photosensor array and fall short in exploiting spatial correlations. Unlike them, CNN2d models emerge as powerful tools for capturing spatial correlations and unraveling complex data patterns. However, their complexity demands intensive computation. As a result, the best option for S1 z -position reconstruction is the developed CNN2d, which achieves a 32 cm error in the z -coordinate. These considerations highlight the need to carefully select the architecture to exploit the symmetries of the data, tailored for effective position reconstruction.

This concludes that the light pattern has been exploited to its fullest, and that the problem should be addressed, as future work, through simulations that also include the time pattern to include both the spatial and temporal aspects of the data.

References

- [1] R. L. Workman *et al.*, “Review of Particle Physics”, *PTEP*, vol. 2022, p. 083C01, 2022. DOI: [10.1093/ptep/ptac097](https://doi.org/10.1093/ptep/ptac097).
- [2] E. Aprile, J. Aalbers, F. Agostini, *et al.*, “Projected WIMP sensitivity of the XENONnT dark matter experiment”, *Journal of Cosmology and Astroparticle Physics*, vol. 2020, pp. 031–031, 2020. DOI: [10.1088/1475-7516/2020/11/031](https://doi.org/10.1088/1475-7516/2020/11/031).
- [3] D. S. Akerib, C. W. Akerlof, S. K. Alsum, *et al.*, “Projected WIMP sensitivity of the LUX-ZEPLIN dark matter experiment”, *Physical Review D*, vol. 101, no. 5, 2020. DOI: [10.1103/physrevd.101.052002](https://doi.org/10.1103/physrevd.101.052002).
- [4] A. M. Green, “Astrophysical uncertainties on direct detection experiments”, *Modern Physics Letters A*, vol. 27, p. 1230004, 2012. DOI: [10.1142/s0217732312300042](https://doi.org/10.1142/s0217732312300042).
- [5] J. H. Oort, *Bull. Astron. Inst. Netherlands*, vol. 6, p. 249, 1932.
- [6] F. Zwicky *et al.*, “The redshift of extragalactic nebulae”, *Helv. Phys. Acta*, vol. 6, p. 138, 1933.
- [7] V. C. Rubin and W. K. Ford Jr, “Rotation of the Andromeda Nebula from a Spectroscopic Survey of Emission Regions”, *Astrophysical Journal*, vol. 159, p. 379, 1970.
- [8] D. Clowe, M. Bradač, A. H. Gonzalez, *et al.*, “A Direct Empirical Proof of the Existence of Dark Matter”, *The Astrophysical Journal*, vol. 648, pp. L109–L113, 2006.
- [9] S. W. Randall, M. Markevitch, D. Clowe, A. H. Gonzalez, and M. Bradač, “Constraints on the Self-Interaction Cross Section of Dark Matter from Numerical Simulations of the Merging Galaxy Cluster 1E 065756”, *The Astrophysical Journal*, vol. 679, pp. 1173–1180, 2008. DOI: [10.1086/587859](https://doi.org/10.1086/587859).
- [10] K. E. Andrade, J. Fuson, S. Gad-Nasr, *et al.*, “A stringent upper limit on dark matter self-interaction cross-section from cluster strong lensing”, *Monthly Notices of the Royal Astronomical Society*, vol. 510, pp. 54–65, 2022.
- [11] N. Aghanim, Y. Akrami, M. Ashdown, *et al.*, “Planck2018 results: VI. Cosmological parameters”, *Astronomy and Astrophysics*, vol. 641, A6, 2020. DOI: [10.1051/0004-6361/201833910](https://doi.org/10.1051/0004-6361/201833910).
- [12] G. Bertone, D. Hooper, and J. Silk, “Particle dark matter: evidence, candidates and constraints”, *Physics Reports*, vol. 405, pp. 279–390, 2005. DOI: [10.1016/j.physrep.2004.08.031](https://doi.org/10.1016/j.physrep.2004.08.031).
- [13] E. Bagnaschi *et al.*, *European Physical Journal C*, vol. 78, p. 8738, 2018.
- [14] J. Rode, “DarkSide: Searching for Dark Matter with Liquid Argon”, Available at HAL <https://theses.hal.science/tel-03924439>, Ph.D. thesis, Sorbonne Université, 2022.
- [15] P. Agnes, I. Albuquerque, T. Alexander, *et al.*, “Simulation of argon response and light detection in the DarkSide-50 dual phase TPC”, *Journal of Instrumentation*, vol. 12, P10015–P10015, 2017. DOI: [10.1088/1748-0221/12/10/p10015](https://doi.org/10.1088/1748-0221/12/10/p10015).
- [16] M. Cárdenas-Montes and R. Santorelli, “Neural Networks for position reconstruction in liquid argon detectors”, *JINST*, vol. 19, p. C05047, 2024. DOI: [10.1088/1748-0221/19/05/C05047](https://doi.org/10.1088/1748-0221/19/05/C05047).

- [17] G. Vera Díaz, R. Santorelli, and V. Pseudo, “Spectral Study of Scintillation and Electroluminescence in Argon Detectors for Direct Dark Matter Detection”, M.S. thesis, 2024.
- [18] I. Rodríguez García, M. Cárdenas-Montes, and R. Santorelli, “Desarrollo de una red neuronal para rechazar eventos de fondo en el detector de materia oscura DEAP-3600”, M.S. thesis, 2019.
- [19] C. Millá Pardo, V. Pseudo, and L. Romero, “Study of the veto system for the DarkSide-20k experiment”, M.S. thesis, 2019.
- [20] M. Misiaszek and N. Rossi, “Direct Detection of Dark Matter: A Critical Review”, *Symmetry*, vol. 16, no. 2, 2024. DOI: [10.3390/sym16020201](https://doi.org/10.3390/sym16020201).
- [21] J. Billard *et al.*, “Direct detection of dark matter - APPEC committee report”, *Reports on Progress in Physics*, vol. 85, pp. 1–106, 2022.
- [22] I. Goodfellow, Y. Bengio, and A. Courville, *Deep Learning*. MIT Press, 2016, Chapters 6 and 9. Available at <http://www.deeplearningbook.org>.
- [23] L. Baudis, S. Profumo, and P. D. Group, “Dark Matter: 27.1 The case for dark matter”, *Physical Review D*, vol. 110, p. 030 001, 2023. [Online]. Available: <https://pdg.lbl.gov/2024/reviews/rpp2024-rev-dark-matter.pdf>.
- [24] DEAP Collaboration, “Machine Learning Approach for Event Position Reconstruction in the DEAP-3600 Dark Matter Search Experiment”, *Physics*, vol. 5, pp. 483–491, 2023. DOI: [10.3390/physics5020033](https://doi.org/10.3390/physics5020033).
- [25] J. Newsom, “Towards Light Charge Association in Liquid Argon Time Projection Chambers”, M.S. thesis, EECS Department, University of California, Berkeley, 2021. [Online]. Available: <http://www2.eecs.berkeley.edu/Pubs/TechRpts/2021/EECS-2021-52.html>.
- [26] P. Agnes, “Direct Detection of Dark Matter with DarkSide-20k”, *EPJ Web of Conferences*, vol. 280, p. 06 003, 2023. DOI: [10.1051/epjconf/202328006003](https://doi.org/10.1051/epjconf/202328006003).
- [27] G. D’Amico, M. Kamionkowski, and K. Sigurdson, “Dark Matter Astrophysics”, 2009. [Online]. Available: <http://arxiv.org/abs/0907.1912>.
- [28] G. D’Amico, M. Kamionkowski, and K. Sigurdson, “Dark Matter Astrophysics”, 2009. DOI: [10.48550/arXiv.0907.1912](https://doi.org/10.48550/arXiv.0907.1912).
- [29] C. E. Aalseth, F. Acerbi, P. Agnes, *et al.*, “DarkSide-20k: A 20 tonne two-phase LAr TPC for direct dark matter detection at LNGS”, *The European Physical Journal Plus*, vol. 133, 2018. DOI: [10.48550/arXiv.1707.08145](https://doi.org/10.48550/arXiv.1707.08145).



MASTER EN FÍSICA; CURSO 2023 – 2024

TUTOR/A: **MIGUEL CÁRDENAS-MONTES**

DEPARTAMENTO: **INVESTIGACIÓN BÁSICA, CIEMAT**

CO-TUTOR/A: **ROBERTO SANTORELLI**

DEPARTAMENTO: **INVESTIGACIÓN BÁSICA, CIEMAT**

TÍTULO DEL TRABAJO:

“Machine Learning models for z-reconstruction in DarkSide-20k experiment”

INTRODUCTION

The nature of dark matter (DM), first proposed by J. Oort and F. Zwicky in the 1930s, is one of the great unresolved questions in modern physics. Several astrophysical observations, from galaxies to the entire universe, strongly suggest its existence and constrain its basic properties. The dominant paradigm assumes DM consists of (relic cold) heavy particles forming halos around galaxies, as described by the Λ CDM model.

Among the several (particle and non-particle) candidates to the missing mass problem, we found potential candidates such as WIMPs -Weakly Interacting Massive Particles-, WIMP-like particles, or light-dark matter. The dark matter particle interacts mostly through gravity and, by definition, via a new weak interaction, making their detection extremely challenging.

In the WIMP theory, there are three main methods to experimentally detect dark matter: direct detection using shielded underground detectors, indirect detection with satellites, balloons, and ground-based telescopes, and collider searches. These complementary approaches are sensitive to different properties and interactions to generate detectable signals. It is worth mentioning that solving the DM enigma may require refining theories, developing more sensitive detection methods, and pushing the boundaries of observational capabilities.

Direct detection searches for DM particles with Earth-based experiments constitutes the most straightforward way of identification. These detectors aim to achieve low energy threshold to detect WIMP collisions with target nuclei and operate in a background-free conditions to identify these very rare events. Various target nuclei and detection techniques are used, with noble gas (e.g., xenon, argon) in single-phase (liquid) or double-phase (liquid-gas) Time Projection Chambers (TPCs) providing the most sensitive results due to their efficient scintillation properties. Both xenon and argon allow for low energy thresholds, and argon is cost-effective to produce due to its abundance in Earth's atmosphere.

GOALS

In this spirit, the Global Argon Dark Matter Collaboration (GADMC) proposes a unified program for liquid argon (LAr) DM direct detection through the DarkSide-20k experiment (DS20k, 200t \times year exposure), a LArTPC detector background-free (< 0.1 events), which has two main signals: scintillation in LAr (S1 signal) and electroluminescence in GAr (S2 signal), and currently under construction. A successful DS20k detector would represent a crucial milestone toward the realization of its successor ARGO (LAr, 3000t \times year exposure), and more specifically the next generation of multi-tonne detectors designed to reach a sensitivity very close to the neutrino floor.



Increasing the target mass and detector volume enhances the event rate but also introduces challenges, such as handling event pile-up. This work explores a possible solution to reduce such loss by developing an algorithm to reconstruct the Z-position from the scintillation signal, S1. This approach aims to improve the accurate association of S1 and S2 pulses for individual events, and so reducing the impact of overlapping signals.

METHODOLOGY

The event Z-reconstruction algorithm is based on DarkSide Monte Carlo (MC) simulations with fixed energy recoils, which provide information about the distribution of S1 light recorded by the arrays of photosensors in our simulated detector, including vertex position coordinates. The algorithm first employs multilayer perceptrons (MLPs, 1D) and then convolutional neural networks (specifically, CNN2D) to exploit spatial correlations of light pattern, using different Deep Learning models to achieve improved accuracy.

BIBLIOGRAPHY

[1] Rode, J. (2022) *DarkSide : Searching for dark matter with liquid argon*. Available at: <https://theses.hal.science/tel-03924439>.

[2] Cárdenas-Montes, M. and Santorelli, R. (2024) *Neural Networks for position reconstruction in liquid argon detectors*.

[3] Vera Díaz, G., Santorelli, R. and Pesudo, V. (2024) *Spectral study of scintillation and electroluminescence in argon detectors for direct dark matter detection*.

[4] Rodríguez García, I., Cárdenas-Montes, M. and Santorelli, R. (2019) *Desarrollo de una red neuronal para rechazar eventos de fondo en el detector de materia oscura DEAP-3600*.

Alumno/a propuesto/a: **NOELIA VICENTE LÓPEZ**

Fdo (Tutor/a):

CARDENAS
MONTES
MIGUEL -
DNI
29480711R

Firmado digitalmente por CARDENAS
MONTES MIGUEL - DNI 29480711R
Nombre de reconocimiento (DN):
c=ES, o=C. INVESTIGACIONES
ENERGETICAS MEDIOAMBIENTALES Y
TECNOLOGICAS, ou=CERTIFICADO
ELECTRONICO DE EMPLEADO
PUBLICO,
serialNumber=IDCES-29480711R,
sn=CARDENAS MONTES,
givenName=MIGUEL, cn=CARDENAS
MONTES MIGUEL - DNI 29480711R
Fecha: 2024.09.18 12:04:00 +02'00'

Fdo (Cotutor/a):

Firmado por SANTORELLI
ROBERTO - DNI ****5912* el día
18/09/2024 con un certificado emitido
por AC Sector Público

Fdo (Alumno/a):

VICENTE
LOPEZ
NOELIA -
48754864Q

Firmado
digitalmente por
VICENTE LOPEZ
NOELIA -
48754864Q
Fecha: 2024.09.17
16:15:24 +02'00'

Madrid, 17 de septiembre de 2024